INTERNATIONAL JOURNAL FOR NUMERICAL METHODS IN FLUIDS, VOL. 24, 1291–1306 (1997)

FINITE ELEMENT ANALYSIS OF AIR FLOW AROUND PERMEABLE SAND FENCES

KATSUMORI HATANAKA* AND SHINTARO HOTTA

Department of Construction Engineering, Nihon University, 7-24-1 Narashino-dai, Funabashi, Chiba 274, Japan

SUMMARY

A numerical study of the turbulent air flow in a trench trap and the turbulent flow around a permeable sand fence is reported in this paper. The two-dimensional modified k–ε turbulence model proposed by Kato and Launder is used to predict the turbulent characteristics of the air flow. The discretization method for the governing equations is the three-step Taylor/Galerkin finite element method proposed by the authors. For the flow in a trench trap the numerical results are compared with experimental data obtained under realistic conditions using a large wind tunnel. For the air flow around a permeable sand fence a pressure loss model is used to represent the effect of the porosity of the fence on the flow field. ©1997 by John Wiley & Sons, Ltd.

Int. J. Numer. Meth. Fluids, **24**: 1291–1306, 1997

No. of Figures: 14. No. of Tables: 0. No. of References: 18.

KEY WORDS: permeable sand fence; trench trap; three-step Taylor/Galerkin method; k–ε turbulence model

1. INTRODUCTION

The coastal areas in Japan are highly utilized for economic purposes, e.g. industry, farming, traffic, recreation and so on. These areas are frequently damaged by intruding wind-blown sand from a neighbouring sandy beach and therefore studies of countermeasures have been performed by many researchers to harness available knowledge for the protection of coastal areas against wind-blown sand damage.[1,2] In order to provide effective and economic protection against wind-blown sand damage, the countermeasure illustrated in Figure 1 has been presented by Hotta.[3] The main point of this countermeasure is that wind-blown sand is caught by a trench trap located beside the foot of an enbankment and the sand caught in the trench is washed away by seawater through a drain. To investigate the efficiency of catching wind-blown sand by a trench, we have performed experiments in a large wind tunnel with various aspect ratios of the trench. In this paper those experimental results are compared with numerical results obtained based upon the modified k–ε turbulence model.

The other objective of this study is the investigation of the efficiency of catching wind-blown sand by a sand fence and a composite of a fence with an embankment. Several experimental and observational studies have been performed in the last few decades.[4,5] In those investigations, however, the primary focus is on the movement of the sand bed and only a few have discussed the turbulent air flow around a sand fence. Since the motion of wind-blown sand is mainly governed by

*Correspondence to: K. Hatanaka, Department of Construction Engineering, Nihon University, 7-24-1 Narashino-dai, Funabashi, Chiba 274, Japan

CCC 0271–2091/97/121291–16 $17.50

Received 1 April 1996
Revised 4 September 1996

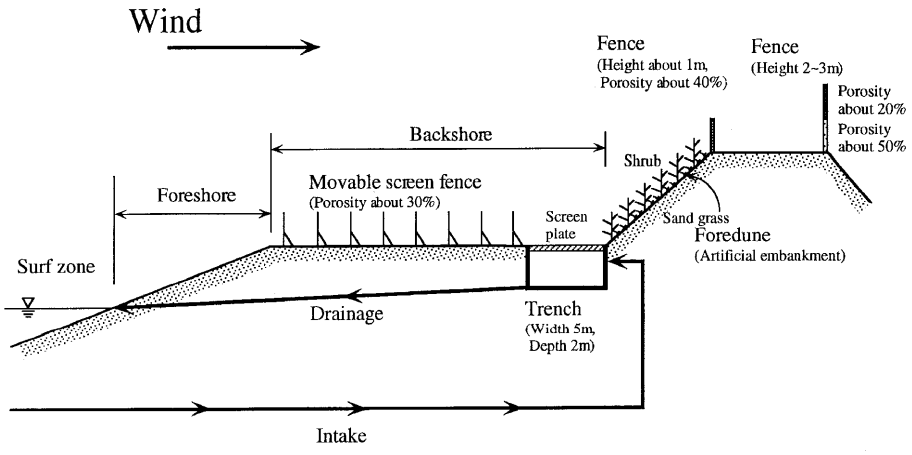

Figure 1. Illustration of countermeasure against wind-blown sand damage[3]

the wind flow itself, we performed numerical simulations of the air flow around a sand fence, including the effect of permeability in the computation. To include the effect of the permeability of an obstacle in a flow field in the computation, Kawamoto and Tanahashi[6] have used Ergun's equation for the numerical estimation of the body force induced by the small-scale flow around pebbles. Toshigami *et al.*[7] have presented the use of the pressure loss term in the numerical simulation of the flow around an automatic guided vehicle. In this modelling the pressure loss term is added to the momentum equation as a supplementary body force term. Both Ergun's equation and the pressure loss term are proportional to the square of the velocity, but Ergun's equation is more complicated than the pressure loss model because it includes some constants defined by experiments. Therefore we selected to use the pressure loss model for the numerical simulations of the air flow around a sand fence including permeability effects.

Even though many turbulent flow simulations have been presented in the literature, the selection of the turbulence model is still important in numerical simulations. In this paper a k–ε model is used for the numerical simulation of the turbulent flow, since the present calculation is limited to two-dimensional computation. Many calculations of turbulent flows which use a k–ε turbulence model have been presented in conjunction with the finite difference method, finite volume method and finite element method.[8–10] According to the literature, the standard k–ε turbulence model gives a very poor prediction of the turbulent characteristics of flows when excessive levels of turbulent energy are calculated in the computation (see e.g. Reference 11). This causes a too high turbulent viscosity and consequently the computed results become unrealistic. To overcome this problem, a number of *modified* k–ε turbulence models have been proposed by several authors.[9–11] In this study we used the modified k–ε turbulence model proposed by Kato and Launder[11] because of its simplicity and efficiency. Details of this are described in the next section.

2. THE TURBULENCE MODEL

Following conventional turbulent flow analysis, the equation of continuity, the Reynolds-averaged Navier–Stokes equation and the k–ε modelling equations for time-dependent, incompressible turbulent flow are

$$\frac{\partial U_i}{\partial x_i}=0, \tag{1}$$

$$\frac{\partial U_i}{\partial t}+U_j\frac{\partial U_i}{\partial x_j}=-\frac{1}{\rho}\frac{\partial P}{\partial x_i}+\frac{\partial}{\partial x_j}\left[(\nu+\nu_t)\left(\frac{\partial U_i}{\partial x_j}+\frac{\partial U_j}{\partial x_i}\right)\right], \tag{2}$$

$$\frac{\partial k}{\partial t}+U_j\frac{\partial k}{\partial x_j}=\frac{\partial}{\partial x_j}\left[\left(\nu+\frac{\nu_t}{\sigma_k}\right)\frac{\partial k}{\partial x_j}\right]+G-\varepsilon, \tag{3}$$

$$\frac{\partial \varepsilon}{\partial t}+U_j\frac{\partial \varepsilon}{\partial x_j}=\frac{\partial}{\partial x_j}\left[\left(\nu+\frac{\nu_t}{\sigma_\varepsilon}\right)\frac{\partial \varepsilon}{\partial x_j}\right]+\frac{\varepsilon}{k}(C_{\varepsilon 1}G-C_{\varepsilon 2}\varepsilon), \tag{4}$$

$$\nu_t=C_\mu\frac{k^2}{\varepsilon}, \tag{5}$$

$$G=\nu_t\left(\frac{\partial U_i}{\partial x_j}+\frac{\partial U_j}{\partial x_i}\right)\frac{\partial U_i}{\partial x_j}. \tag{6}$$

Here U_i and P are the local time-averaged velocity components and pressure respectively, k and ε are the turbulent kinetic energy and its dissipation rate respectively, ν is the kinematic viscosity, ν_t is the turbulent eddy viscosity and G is the turbulence production term. The values of the constants C_μ, $C_{\varepsilon 1}$, $C_{\varepsilon 2}$, σ_k and σ_ε used in the turbulence model are 0·09, 1·44, 1·92, 1·0 and 1·3 respectively.[8]

These formulations, however, are known to give very poor predictions of turbulent characteristics when excessive generation of turbulent energy leads to a too high turbulent viscosity. To overcome this, Kato and Launder[11] have presented a modified k–ε model. Let the dimensionless strain parameter S and vorticity parameter Ω be

$$S=\sqrt{\left[\frac{1}{2}\left(\frac{\partial U_i}{\partial x_j}+\frac{\partial U_j}{\partial x_i}\right)^2\right]}, \tag{7}$$

$$\Omega=\sqrt{\left[\frac{1}{2}\left(\frac{\partial U_i}{\partial x_j}-\frac{\partial U_j}{\partial x_i}\right)^2\right]}. \tag{8}$$

From equation (6) it is easily verified that the energy production term is rewritten as

$$G=\nu_t S^2. \tag{9}$$

Near a stagnation point the very high value of S leads to excessive levels of G. However, the vorticity parameter Ω near a stagnation point becomes nearly equal to zero, since the deformation is nearly irrotational. Thus the replacement

$$G=\nu_t S\Omega \tag{10}$$

gives a substantial diminution of G in the region of a stagnation point. This idea has been found to give a satisfactory prediction in the computation of turbulent flows.[11] The modification is no panacea for the ills of the Bousinessq stress–strain hypothesis, but it does greatly improve the behaviour in some flows.

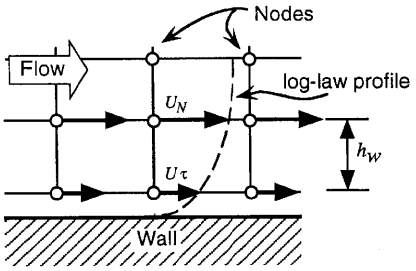

Figure 2. Boundary condition defined by wall function

3. BOUNDARY CONDITIONS

In typical problems simulated by the k–ε model, the wall function method proposed by Launder and Spalding[8] is used. According to this method, the velocity profile in the turbulent boundary layer near a smooth wall gives the following *slip* tangential velocity boundary conditions along the wall:

$$u^+ = y^+ \quad \text{when} \quad y^+ < 11{\cdot}6, \tag{11}$$

$$u^+ = \frac{1}{\kappa}\ln(9y^+) \quad \text{when} \quad y^+ \geq 11{\cdot}6, \tag{12}$$

$$u^+ = U_\tau/u_*, \qquad y^+ = h_w u_*/\nu. \tag{13}$$

Here U_τ and h_w are the tangential velocity component along the wall and the mesh length respectively (see Figure 2), κ is von Karman's constant, taken to be 0·41, and the friction velocity u_* is obtained from the log-law velocity profile

$$|U_N| = \frac{u_*}{\kappa}\ln\left(\frac{9h_w u_*}{\nu}\right), \tag{14}$$

where U_N is the tangential velocity component along the wall as described in Figure 2. The normal velocity component U_n is also specified as

$$U_n = 0 \tag{15}$$

on the wall boundary. The boundary conditions for k and ε are imposed local equilibrium conditions near the wall represented as

$$k = \frac{u_*^2}{C_\mu^{1/2}}, \qquad \varepsilon = \frac{u_*^3}{\kappa h_w}. \tag{16}$$

At the inlet, U_i, k and ε are imposed as

$$U_i = \hat{U}_i, \qquad k = \hat{k}, \qquad \varepsilon = \hat{\varepsilon}, \tag{17}$$

where a 'hat' denotes a given value on the boundary. At the exit the traction-free condition is assumed for the mean flow quantities and the normal gradients of k and ε are imposed as zero. The boundary conditions stated above can be expressed as

$$\left[-\frac{1}{\rho}P\delta_{ij} + (\nu+\nu_t)\left(\frac{\partial U_i}{\partial x_j} + \frac{\partial U_j}{\partial x_i}\right)\right]\cdot n_i = 0, \qquad \frac{\partial k}{\partial n_i} = 0, \qquad \frac{\partial \varepsilon}{\partial n_i} = 0, \tag{18}$$

where n_i is the unit vector of the direction cosine.

4. THREE-STEP TAYLOR/GALERKIN METHOD

The discretization strategy used in this paper is the *three-step Taylor/Galerkin method*.[12,13] In this strategy the pressure Poisson equation is derived in the following manner. Let U_i be the known variables of the velocity field at time $t^n = t^{n-1} + \Delta t$ ($n = 1, 2, \ldots$), where Δt is the time increment. Then the unknown velocity variable U_i^{n+1} can be calculated from the discretized Reynolds-averaged Navier–Stokes equation that is discretized in time by the forward Euler finite difference scheme:

$$\frac{U_i^{n+1} - U_i^n}{\Delta t} + U_j^n \frac{\partial U_i^n}{\partial x_j} = -\frac{1}{\rho}\frac{\partial P^{n+1}}{\partial x_i} + \frac{\partial}{\partial x_j}\left[(\nu + \nu_t^n)\left(\frac{\partial U_i^n}{\partial x_j} + \frac{\partial U_j^n}{\partial x_i}\right)\right]. \tag{19}$$

The incompressibility constraint (1) is forced to be satisfied in the $n+1$ time stage as

$$\frac{\partial U_i^{n+1}}{\partial x_i} = 0. \tag{20}$$

After taking the divergence of both sides of (19) then substituting (20), the following pressure Poisson equation can be derived:

$$\frac{1}{\rho}\frac{\partial^2 P^{n+1}}{\partial x_{ii}^2} = \frac{1}{\Delta t}\frac{\partial U_i^n}{\partial x_i} - \frac{\partial U_j^n}{\partial x_i}\frac{\partial U_i^n}{\partial x_j} - U_j^n \frac{\partial^2 U_i^n}{\partial x_i \partial x_j} + \frac{\partial^2}{\partial x_i \partial x_j}\left[(\nu + \nu_t^n)\left(\frac{\partial U_i^n}{\partial x_j} + \frac{\partial U_j^n}{\partial x_i}\right)\right] \tag{21}$$

The boundary conditions for this are

$$P^{n+1} = \hat{P}, \qquad \frac{\partial P^{n+1}}{\partial x_i} = \hat{\gamma}_i. \tag{22}$$

Once the pressure field has been calculated from (21), the velocity U_i^{n+1} can be computed from (19), which can be treated as a convection–diffusion equation.

Many solution techniques for Burgers-type equations have been presented in the last decade, especially for the convection-dominated flow situation.[14–16] The Taylor/Galerkin method is one of the solution strategies for convection-dominated flow that was first presented by Selmin *et al*.[17] This method provides a third-order-accurate result in space and time with good stability when the Courant number is less than 1·0. The advantage of using the Taylor/Galerkin method is that the specification of special computational parameters, often required in other stabilized strategies so that the computation may be stable, is not required at all. However, this method includes third-order derivative terms and this is undesirable for linear interpolation functions. We have therefore proposed a three-step Taylor/Galerkin method which does not have higher-order derivative terms but retains the benefit obtained from the original Taylor/Galerkin method. Details of the present method can be found in Reference 13.

By making use of the three-step Taylor/Galerkin method, the momentum equation, pressure Poisson equation and k- and ε-equations can be discretized as follows.

Step 1

$$U_i^{n+1/3} = U_i^n - \frac{\Delta t}{3}\left\{U_j^n \frac{\partial U_i^n}{\partial x_j} + \frac{1}{\rho}\frac{\partial P^n}{\partial x_i} - \frac{\partial}{\partial x_j}\left[(\nu + \nu_t^n)\left(\frac{\partial U_i^n}{\partial x_j} + \frac{\partial U_j^n}{\partial x_i}\right)\right]\right\}, \tag{23}$$

$$k^{n+1/3} = k^n - \frac{\Delta t}{3}\left\{U_j^n \frac{\partial k^n}{\partial x_j} - \frac{\partial}{\partial x_j}\left[\left(\nu + \frac{\nu_t^n}{\sigma_k}\right)\frac{\partial k^n}{\partial x_j}\right] + G^n - \varepsilon^n\right\}, \tag{24}$$

$$\varepsilon^{n+1/3} = \varepsilon^n - \frac{\Delta t}{3}\left\{U_j^n \frac{\partial \varepsilon^n}{\partial x_j} - \frac{\partial}{\partial x_j}\left[\left(\nu + \frac{\nu_t^n}{\sigma_\varepsilon}\right)\frac{\partial \varepsilon^n}{\partial x_j}\right] + \frac{\varepsilon^n}{k^n}\left(C_{\varepsilon 1} G^n - C_{\varepsilon 2}\varepsilon^n\right)\right\}. \tag{25}$$

Step 2

$$U_i^{n+2/3} = U_i^n - \frac{\Delta t}{2}\left\{U_j^{n+1/3} \frac{\partial U_i^{n+1/3}}{\partial x_j} + \frac{1}{\rho}\frac{\partial P^n}{\partial x_i} - \frac{\partial}{\partial x_j}\left[(\nu + \nu_t^{n+1/3})\left(\frac{\partial U_i^{n+1/3}}{\partial x_j} + \frac{\partial U_j^{n+1/3}}{\partial x_i}\right)\right]\right\}, \tag{26}$$

$$k^{n+2/3} = k^n - \frac{\Delta t}{2}\left\{U_j^{n+1/3} \frac{\partial k^{n+1/3}}{\partial x_j} - \frac{\partial}{\partial x_j}\left[\left(\nu + \frac{\nu_t^{n+1/3}}{\sigma_k}\right)\frac{\partial k^{n+1/3}}{\partial x_j}\right] + G^{n+1/3} - \varepsilon^{n+1/3}\right\}, \tag{27}$$

$$\varepsilon^{n+2/3} = \varepsilon^n - \frac{\Delta t}{2}\left\{U_j^{n+1/3} \frac{\partial \varepsilon^{n+1/3}}{\partial x_j} - \frac{\partial}{\partial x_j}\left[\left(\nu + \frac{\nu_t^{n+1/3}}{\sigma_\varepsilon}\right)\frac{\partial \varepsilon^{n+1/3}}{\partial x_j}\right] + \frac{\varepsilon^{n+1/3}}{k^{n+1/3}}\left(C_{\varepsilon 1} G^{n+1/3} - C_{\varepsilon 2}\varepsilon^{n+1/3}\right)\right\}. \tag{28}$$

Step 3

$$\frac{1}{\rho}\frac{\partial^2 P^{n+1}}{\partial x_{ii}^2} = \frac{1}{\Delta t}\frac{\partial U_i^n}{\partial x_i} - \frac{\partial U_j^{n+2/3}}{\partial x_i}\frac{\partial U_i^{n+2/3}}{\partial x_j} - U_j^{n+2/3}\frac{\partial^2 U_i^{n+2/3}}{\partial x_i \partial x_j} + \frac{\partial^2}{\partial x_i \partial x_j}\left[(\nu + \nu_t^{n+2/3})\left(\frac{\partial U_i^{n+2/3}}{\partial x_j} + \frac{\partial U_j^{n+2/3}}{\partial x_i}\right)\right], \tag{29}$$

$$U_i^{n+1} = U_i^n - \Delta t\left\{U_j^{n+2/3} \frac{\partial U_i^{n+2/3}}{\partial x_j} + \frac{1}{\rho}\frac{\partial P^{n+1}}{\partial x_i} - \frac{\partial}{\partial x_j}\left[(\nu + \nu_t^{n+2/3})\left(\frac{\partial U_i^{n+2/3}}{\partial x_j} + \frac{\partial U_j^{n+2/3}}{\partial x_i}\right)\right]\right\}, \tag{30}$$

$$k^{n+1} = k^n - \Delta t\left\{U_j^{n+2/3} \frac{\partial k^{n+2/3}}{\partial x_j} - \frac{\partial}{\partial x_j}\left[\left(\nu + \frac{\nu_t^{n+2/3}}{\sigma_k}\right)\frac{\partial k^{n+2/3}}{\partial x_j}\right] + G^{n+2/3} - \varepsilon^{n+2/3}\right\}, \tag{31}$$

$$\varepsilon^{n+1} = \varepsilon^n - \Delta t\left\{U_j^{n+2/3} \frac{\partial \varepsilon^{n+2/3}}{\partial x_j} - \frac{\partial}{\partial x_j}\left[\left(\nu + \frac{\nu_t^{n+2/3}}{\sigma_\varepsilon}\right)\frac{\partial \varepsilon^{n+2/3}}{\partial x_j}\right] + \frac{\varepsilon^{n+2/3}}{k^{n+2/3}}\left(C_{\varepsilon 1} G^{n+2/3} - C_{\varepsilon 2}\varepsilon^{n+2/3}\right)\right\}. \tag{32}$$

In these formulations the variables superscripted $n+1/3$ and $n+2/3$ stand for the intermediate variables of corresponding variables. The use of the standard Galerkin method with the bilinear isoparametric finite element yields the following finite element formulations.

Step 1

$$\mathbf{MU}^{n+1/3} = \mathbf{MU}^n - \frac{\Delta t}{3}(\mathbf{KU}^n + \mathbf{HP}^n + \mathbf{SU}^n), \tag{33}$$

$$\mathbf{Mk}^{n+1/3} = \mathbf{Mk}^n - \frac{\Delta t}{3}(\mathbf{Kk}^n + \mathbf{S}_k\mathbf{k}^n - \mathbf{G}^n + \mathbf{M}\varepsilon^n), \tag{34}$$

$$\mathbf{M}\varepsilon^{n+1/3} = \mathbf{M}^n - \frac{\Delta t}{3}\left[\mathbf{K}\varepsilon^n + \mathbf{S}_\varepsilon\varepsilon^n - \overline{\left(\frac{k^n}{\varepsilon^n}\right)}(C_{\varepsilon 1}\mathbf{G}^n - C_{\varepsilon 2}\mathbf{M}\varepsilon^n)\right]. \tag{35}$$

Step 2

$$\mathbf{MU}^{n+2/3} = \mathbf{MU}^n - \frac{\Delta t}{2}(\mathbf{KU}^{n+1/3} + \mathbf{HP}^n + \mathbf{SU}^{n+1/3}), \tag{36}$$

$$\mathbf{Mk}^{n+2/3} = \mathbf{Mk}^n - \frac{\Delta t}{2}(\mathbf{Kk}^{n+1/3} + \mathbf{S}_k\mathbf{k}^{n+1/3} - \mathbf{G}^{n+1/3} + \mathbf{M}\varepsilon^{n+1/3}), \tag{37}$$

$$\mathbf{M}\varepsilon^{n+2/3} = \mathbf{M}^n - \frac{\Delta t}{2}\left[\mathbf{K}\varepsilon^{n+1/3} + \mathbf{S}_\varepsilon\varepsilon^{n+1/3} - \overline{\left(\frac{k^{n+1/3}}{\varepsilon^{n+1/3}}\right)}(C_{\varepsilon 1}\mathbf{G}^{n+1/3} - C_{\varepsilon 2}\mathbf{M}\varepsilon^{n+1/3})\right]. \tag{38}$$

Step 3

$$\mathbf{MU}^{n+1} = \mathbf{MU}^n - \Delta t(\mathbf{KU}^{n+2/3} + \mathbf{HP}^{n+1} + \mathbf{SU}^{n+2/3}), \tag{39}$$

$$\mathbf{Mk}^{n+1} = \mathbf{Mk}^n - \Delta t(\mathbf{Kk}^{n+2/3} + \mathbf{S}_k\mathbf{k}^{n+2/3} - \mathbf{G}^{n+2/3} + \mathbf{M}\varepsilon^{n+2/3}), \tag{40}$$

$$\mathbf{M}\varepsilon^{n+1} = \mathbf{M}^n - \Delta t\left[\mathbf{K}\varepsilon^{n+2/3} + \mathbf{S}_\varepsilon\varepsilon^{n+2/3} - \overline{\left(\frac{k^{n+2/3}}{\varepsilon^{n+2/3}}\right)}(C_{\varepsilon 1}\mathbf{G}^{n+2/3} - C_{\varepsilon 2}\mathbf{M}\varepsilon^{n+2/3})\right]. \tag{41}$$

Here **M**, **K**, **S** and **H** are the mass matrix, convection matrix, diffusion matrix and gradient matrix respectively. The line integral terms to be treated as the *natural* boundary conditions are omitted. The proper treatment of the natural boundary conditions is discussed in Reference 18.

5. RESULTS AND DISCUSSION

5.1. Flow in a trench trap

In order to investigate the flow behaviour in a trench trap, experiments were carried out using a blow-off type of wind tunnel which was specially designed for wind-blown sand at the Central Research Institute of Electronic Power Industry, Abiko, Japan. The wind tunnel has a test section 110 cm high, 100 cm wide and 20 m long. The wind speed is variable from 3 to 30 m s^{-1}, controlled by the frequency of a rotary fan. An ultrasonic anemometer array with 15 anemometers was used for measuring the wind speed. The trench depth is fixed as $H = 20$ cm in the experiments and the inflow wind speeds were set to 5, 8 and 15 m s^{-1}. The Reynolds numbers of the experiments were about 7×10^4, $1{\cdot}1 \times 10^5$ and 2×10^5 respectively. Experiments with trench aspect ratios $B/H = 2$, 4, 6, 8 and 10 were carried out. The definition of the trench aspect ratio and a sketch of the computational domain are illustrated in Figure 3. In the numerical simulation the Reynolds number is fixed as 10^5 and simulations with aspect ratos $B/H = 4$ and 6 were examined. In the computation for $B/H = 4$ we have used the two finite element meshes shown in Figure 4 to check the effect of mesh refinement. Mesh A in Figure 4 has 8365 nodes and 8160 elements and becomes gradually finer towards the wall and bottom of the trench trap. Mesh B has 12,425 nodes and 12,160 elements and is also gradually refined towards the bottom, but not refined at the level of the bottom of the trench trap. Figure 5 and 6

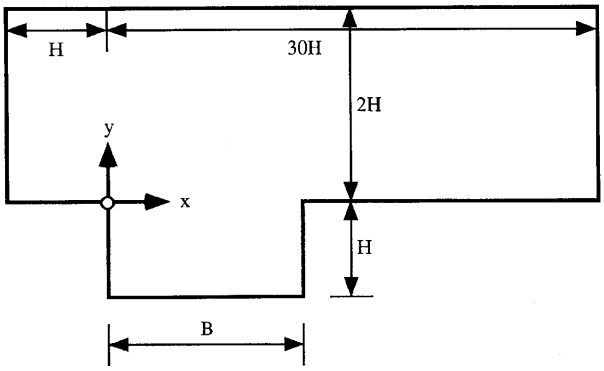

Figure 3. Definition sketch of computational domain and aspect ratio of trench (B/H)

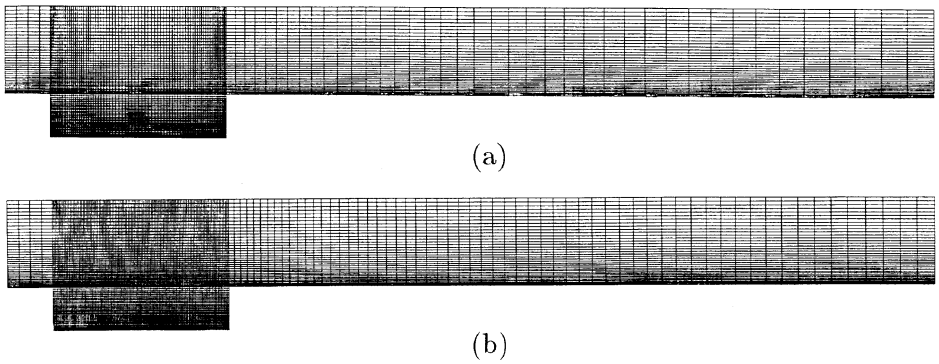

Figure 4. Finite element meshes for $B/H=4$: (a) mesh A (8365 nodes and 8160 elements); (b) mesh B (12,425 nodes and 12,160 elements)

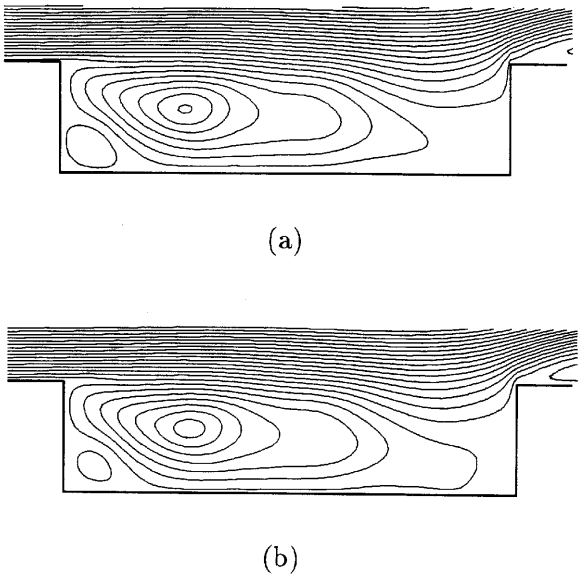

Figure 5. Streamlines of mean velocity field computed using (a) mesh A and (b) mesh B ($Re=10^5$, $B/H=4$)

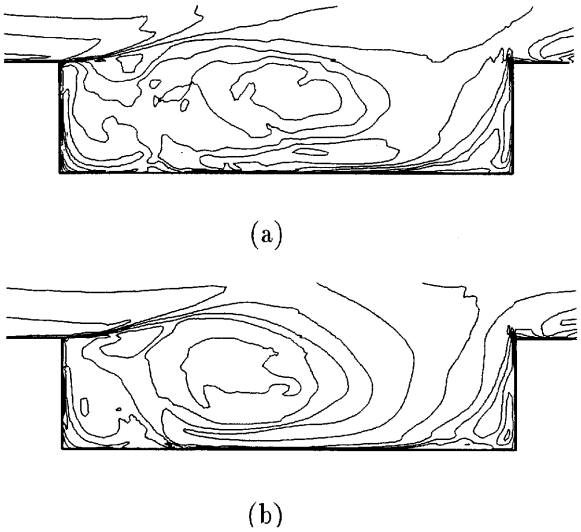

Figure 6. Distributions of mean turbulent kinetic energy computed using (a) mesh A and (b) mesh B ($Re = 10^5$, $B/H = 4$)

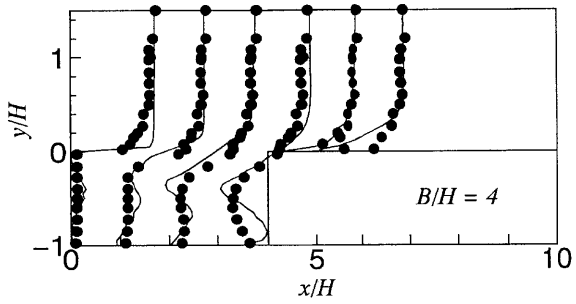

Figure 7. Comparison of $|U_i|$ for $B/H = 4$: ●, experiment; ————, numerical result

show the computed streamlines and distributions of turbulent kinetic energy respectively using the two meshes. No clear difference is seen between the results of the different meshes. Figure 7 shows a comparison of the velocity magnitude $|U_i|$ obtained by experiments and numerical simulations for $B/H = 4$. The magnitudes of the velocity profiles are normalized by the inflow wind speed value. The mainstream velocity profiles of experiments and simulations are in good agreement with each other. However, the vortex in the trench computed numerically is rather large than that of experiments. This is presumed to be caused by the lack of a three-dimensional effect of the flow field in the present numerical simulation. The finite element mesh for $B/H = 6$ is shown in Figure 8(a) and the computed streamlines in the trench are shown in Figure 8(b). Because the aspect ratio of the trench has changed from 4 to 6, the vortex centre of the mainstream in the trench has moved downstream. Figure 8(c) shows the same comparison as Figure 7 for $B/H = 6$. The computed results are in good agreement with the experimental results in the mainstream, but the computed vortex in the trench is also larger than that of experiments. The same reason as in the case of $B/H = 4$ is considered responsible.

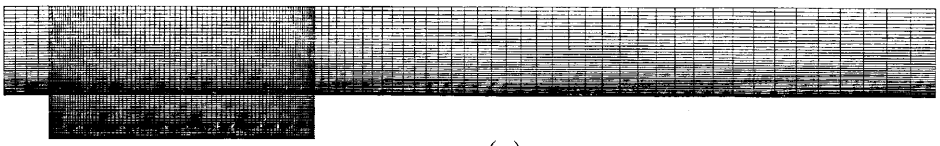

(a)

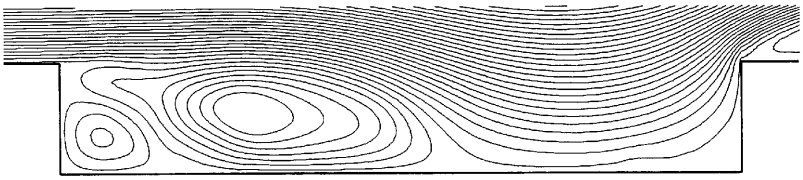

(b)

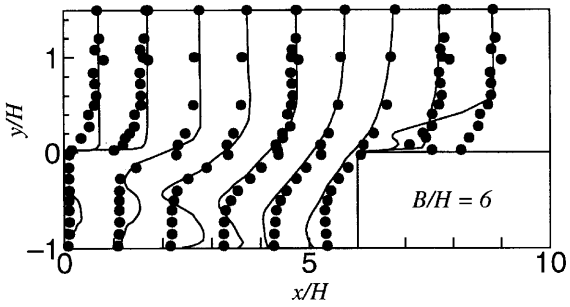

(c)

Figure 8. Finite element mesh and computed results ($Re=10^5$, $B/H=6$). (a) Finite element mesh (8365 nodes and 8160 elements). (b) Streamlines of mean velocity field. (c) Comparison of $|U_i|$ for $B/H=6$: ●, experiment; ————, numerical result

5.2. *Flow around permeable sand fences*

As mentioned previously, the pressure loss modelling presented by Toshigami *et al.*[7] has been utilized to include the permeability effect of the sand fence in the numerical computation. The pressure loss term used in this study is defined by the equations

$$F=\frac{\Delta P}{\Delta x_e}, \qquad \Delta P=\frac{K}{2}|U_j|U_j, \tag{42}$$

where Δx_e is the mesh length of fence elements and K is the coefficient of resistance calculated from

$$K=C_S\frac{1-\alpha}{\alpha^2}. \tag{43}$$

Here α is the porosity of the fence under consideration and C_S is a coefficient determined from the shape of the fence and the Reynolds number of the flow. In this study, C_S is fixed as 1·3. The pressure loss term is added to the momentum equation as a supplementary body force term. A sketch of the

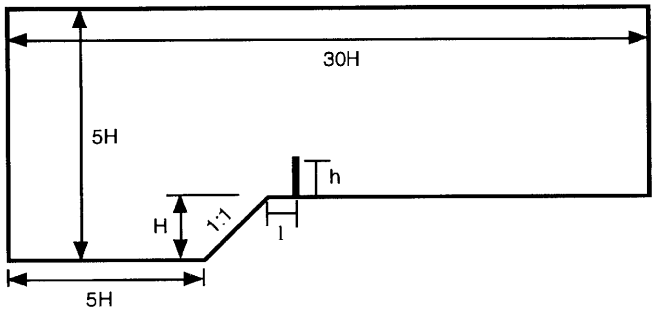

Figure 9. Definition sketch of computational domain of air flow around sand fence

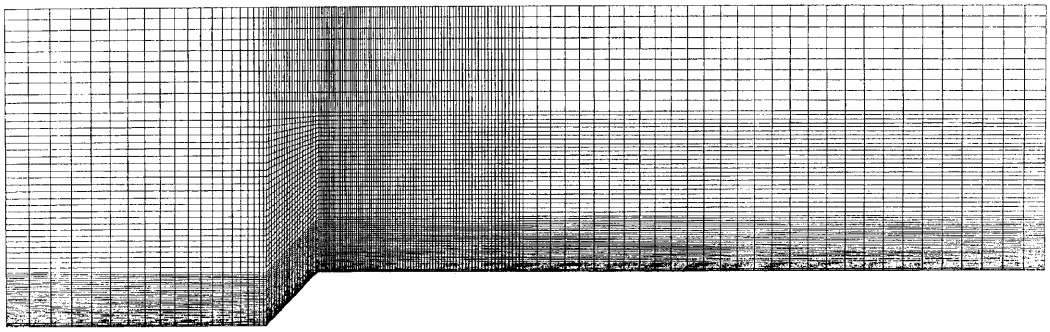

Figure 10. Finite element mesh (11,476 nodes and 11,250 elements)

computational domain is shown in Figure 9. Figure 10 shows the finite element mesh used in this computation. The total numbers of nodes and elements are 11,476 and 11,250 respectively. The simulations were carried out with various values of the porosity of the fence, α, and the height of the fence, h. The Reynolds number of all cases is imposed as $Re = 10^5$. The computed streamlines and distributions of turbulent kinetic energy of each case are shown in Figures 11–14.

The flow field does not change much when the porosity of the sand fence is changed. A drastic change in flow can be observed upon changing the height of the fence. This means that the frequency of vortex shedding from the edge of the embankment is changing owing to the change in the resistance force of the fence. Another observation is that the change in the frequency of vortex shedding changes the distribution of turbulent kinetic energy, especially near the slope of the embankment, where a small recirculation area of flow can be observed. This means that the turbulent viscosity computed from the modified k–ε model is not producing a too high turbulent viscosity in the computation of the counter-gradient pressure flow, whereas the standard k–ε model always produces an unrealistic turbulent viscosity. Therefore, the replacement of the production term G by (10) is working successfully.

6. CONCLUSIONS

Numerical simulations of the turbulent flow in a trench trap and the flow around a permeable sand fence were carried out by the three-step Taylor/Galerkin finite element method in conjunction with a

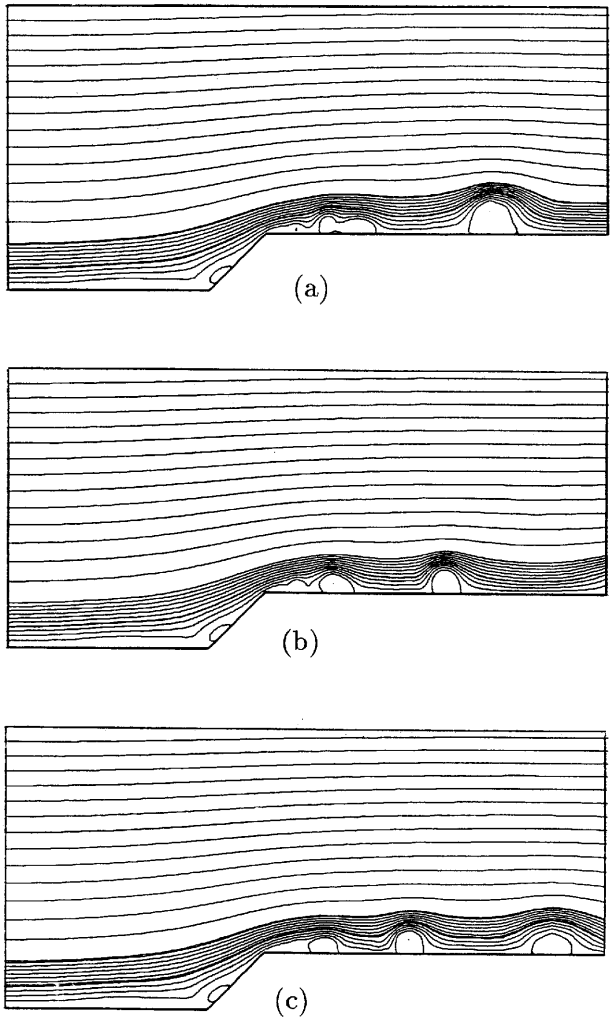

Figure 11. Computed streamlines ($Re = 10^5$): (a) $\alpha = 1{\cdot}0$ (corresponding to case of no fence); (b) $\alpha = 0{\cdot}5$, $h = 0{\cdot}2$, $l = 0{\cdot}0$; (c) $\alpha = 0{\cdot}3$, $h = 0{\cdot}2$, $l = 0{\cdot}0$

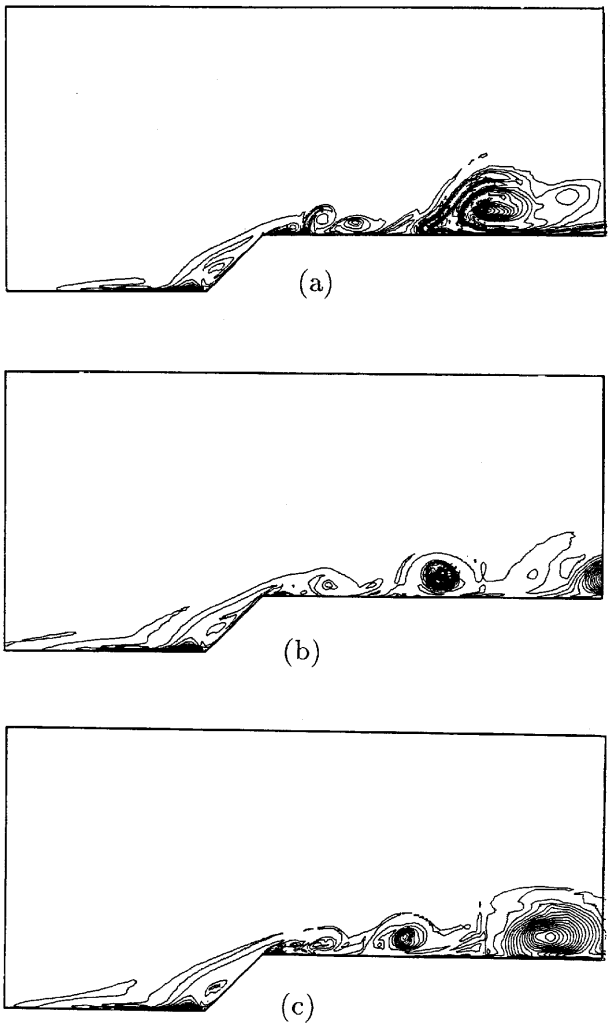

Figure 12. Distributions of k ($Re = 10^5$): (a) $\alpha = 1{\cdot}0$; (b) $\alpha = 0{\cdot}5$, $h = 0{\cdot}2$, $l = 0{\cdot}0$; (c) $\alpha = 0{\cdot}3$, $h = 0{\cdot}2$, $l = 0{\cdot}0$

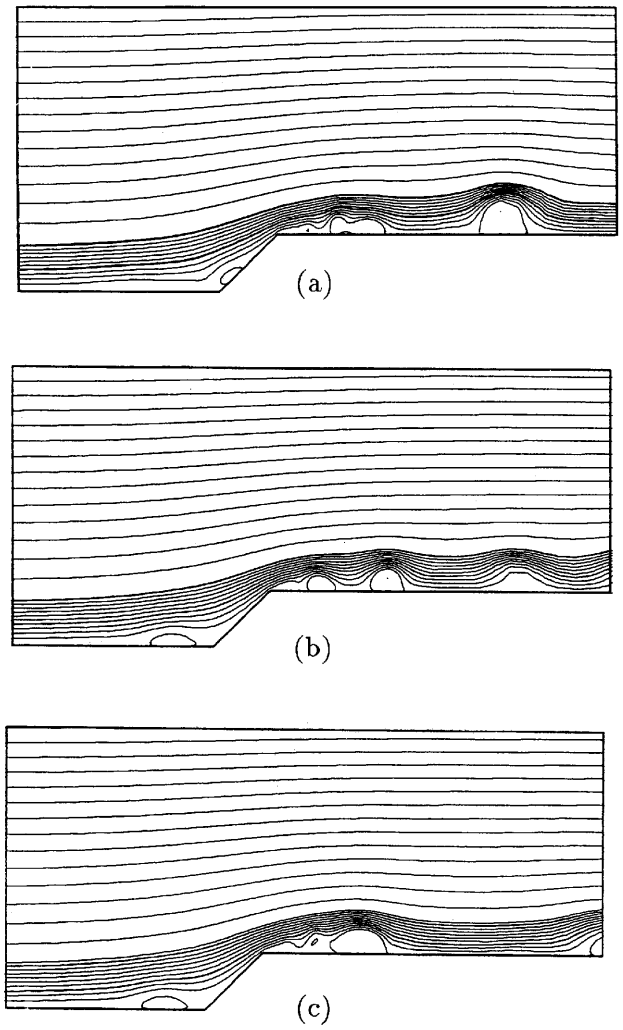

Figure 13. Computed streamlines ($Re = 10^5$): (a) $\alpha = 1{\cdot}0$ (corresponding to case of no fence); (b) $\alpha = 0{\cdot}5$, $h = 1{\cdot}0$, $l = 0{\cdot}0$; (c) $\alpha = 0{\cdot}3$, $h = 1{\cdot}0$, $l = 0{\cdot}0$

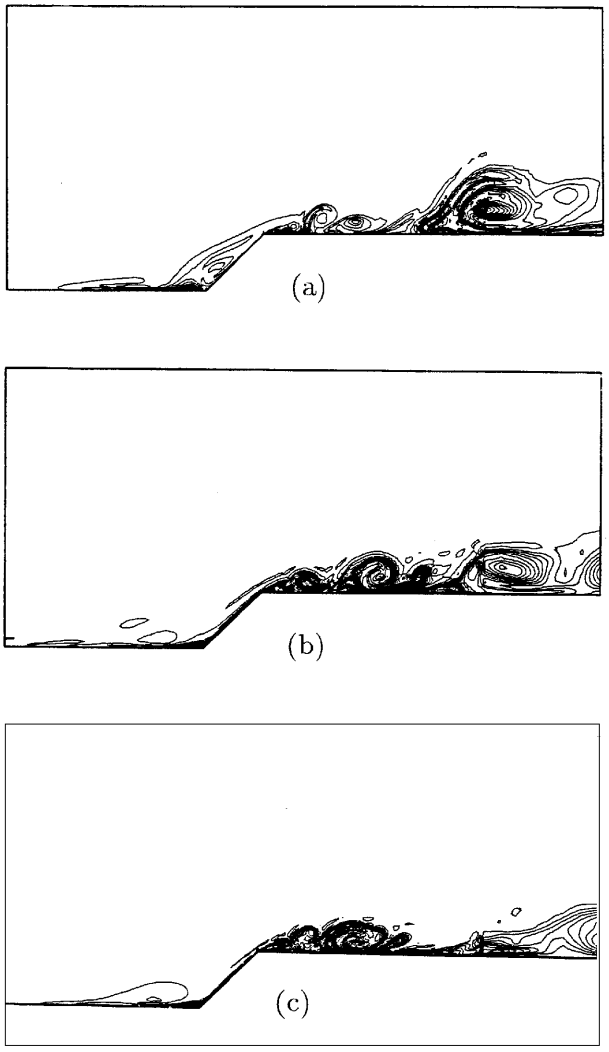

Figure 14. Distributions of k ($Re = 10^5$): (a) $\alpha = 1{\cdot}0$; (b) $\alpha = 0{\cdot}5$, $h = 1{\cdot}0$, $l = 0{\cdot}0$; (c) $\alpha = 0{\cdot}3$, $h = 1{\cdot}0$, $l = 0{\cdot}0$

modified k–ε turbulence model. In the computation of the air flow in a trench trap the computed and experimental results are practically in good agreement with each other. For engineering purposes the above shows that the present method is applicable to the problem discussed here. However, 2D computation cannot predict the flow situation exactly so far. 3D computation is required in the numerical simulation of the strict behaviour of the turbulent flow situation. In the computation of the air flow around a permeable sand fence the pressure loss modelling works reasonably well. The effect of introducing the production term proposed by the modified k–ε turbulence model is also verified.

Three-dimensional computations, comparison of the computed results around a sand fence with experiments and flow analysis around the whole countermeasure illustrated in Figure 1 are future subjects of this study.

ACKNOWLEDGEMENT

The authors are grateful to the Central Research Institute of the Electric Power Industry for its support over the course of this work.

REFERENCES

1. K. Horikawa, S. Hotta, S. Kubota and K. Katori, 'Field measurement of blown sand transport rate by trench trap', *Coastal Eng. Jpn.*, **27**, 213–232 (1984).
2. K. Horikawa, S. Hott and N. C. Kraus, 'Literature review of sand transport by wind on a dry sand surface', *Coastal Eng.*, **9**, 503–526 (1986).
3. S. Hotta, 'Countermeasures for controlling wind-blown sand: a summary of current methods and an introduction to a new method', *Proc. Int. Conf. on Coastal Zone in Canada '94*, 1994, p. 2287.
4. S. Hotta, N. C. Kraus and K. Horikawa, 'Function of sand fences in controlling wind-blown sand', *Proc. Coastal Sediments '87*, ASCE, 1987, pp. 772–787.
5. S. Hotta and K. Horikawa, 'Function of sand fence placed in front of embankment', *Proc. 22nd Coastal Engineer in Conf.*, ASCE, 1990, pp. 2754–2767.
6. S. Kawamoto and T. Tanahashi, 'Numerical analysis of moving-bed heat exchanger using high-speed GSMAC-FEM', *Trans. Jpn. Soc. Mech. Eng.*, **57**, 282–287 (1991) (in Japanese).
7. K. Toshigami, Y. Tashiro, H. Kanayama, S. Fujima and M. Tabata, 'Finite element analysis of air flow around an automatic guided vehicle', *Proc. 5th Japan CFD Symp.*, 1991, pp. 613–616 (in Japanese).
8. B. E. Launder and D. B. Spalding, 'The numerical computation of turbulent flow', *Comput, Methods Appl. Mech. Eng.*, **3**, 269– 289 (1974).
9. S. Kawamoto, 'An improved k–ε turbulence model on high-speed GSMAC-FEM for estimation of wind load', *Proc. 2nd Japan- -U.S. Symp. on Finite Element Methods in Large-Scale Computational Fluid Dynamics*, 1994, pp. 105–108.
10. S. Murakami, 'Computational wind engineering', *J. Wind Eng. Ind. Aerodyn.*, **35**, 517 (1990).
11. M. Kato and B. E. Launder, 'The modelling of turbulent flow around stationary and vibrating square cylinder', *Proc. 9th Symp. on Turbulent Shear Flows*, 1993, pp. 10-4-1–10-4-6.
12. K. Hatanaka, 'A numerical study on vortex shedding around a heated/cooled circular cylinder by three-step Taylor–Galerkin method', *Proc. 2nd Japan–U.S. Symp. on Finite Element Methods in Large- Scale Computational Fluid Dynamics*, 1994, pp. 109–112.
13. C. B. Jiang, K. Hatanaka, M. Kawahara and K. Kashiyama, 'A three-step finite element method for convection dominated incompressible flow', *Comput. Fluid Dyn. J.*, **1**, 447 (1993).
14. A. N. Brooks and T. J. R. Hughes, 'Streamline upwind/Petrov– Galerkin formulations for convection dominated flows with particular emphasis on the incompressible Navier–Stokes equations', *Comput. Methods Appl. Mech. Eng.*, **32**, 199 (1982).
15. J. Donea, S. Giuliani and L. Quartapelle, 'Time-accurate solution of advection–diffusion problems', *J. Comput. Phys.*, **70**, 463– 499 (1987).
16. M. Kawahara, 'Convergence of finite element Lax–Wendroff method for linear hyperbolic differential equation', *Proc. JSCE*, **253**, 95 (1976).
17. V. Selmin, J. Donea and L. Quartapelle, 'Finite element methods for nonlinear advection', *Comput. Methods Appl. Mech. Eng.*, **52**, 817–845 (1985).
18. K. Hatanaka and M. Kawahara, 'A fractional step finite element method for conductive–convective heat transfer problem', *Int. J. Numer. Methods Heat Fluid Flow*, **1**, 77–94 (1991).

